

Atomic structures of Ruddlesden-Popper faults in $\text{LaCoO}_3/\text{SrRuO}_3$ multilayer thin films induced by epitaxial strain

Wei Wang^{a,b}, Hui Zhang^{a,b}, Xi Shen^a, Xiangxiang Guan^{a,b}, Yuan Yao^a, Yanguo Wang^a, Jirong Sun^{a,b}, Richeng Yu^{a,b,*}

^a Beijing National Laboratory of Condensed Matter Physics, Institute of Physics, Chinese Academy of Sciences, Beijing 100190, PR China

^b School of Physical Sciences, University of Chinese Academy of Sciences, Beijing 100049, PR China

ARTICLE INFO

Article history:

Received 30 September 2017

Received in revised form 8 January 2018

Accepted 19 March 2018

Available online 20 March 2018

Communicated by M.S. Goorsky

Keywords:

A1. Crystal structure

A1. Defects

A1. Stresses

A3. Thin film growth

B2. Magnetic materials

A1. Scanning transmission electron microscopy

ABSTRACT

In this paper, scanning transmission electron microscopy is used to study the microstructures of the defects in $\text{LaCoO}_3/\text{SrRuO}_3$ multilayer films grown on the SrTiO_3 substrates, and these films have different thickness of SrRuO_3 (SRO) layers. Several types of Ruddlesden–Popper (R.P.) faults at an atomic level are found, and these chemical composition fluctuations in the growth process are induced by strain fields originating from the film–film and film–substrate lattice mismatches. Furthermore, we propose four types of structural models based on the atomic arrangements of the R.P. planar faults, which severely affect the functional properties of the films.

© 2018 Elsevier B.V. All rights reserved.

1. Introduction

The oxide thin film with perovskite structure has recently received extensive attention because of its unusual physical properties, such as interfacial two-dimensional (2D) conductivity [1], strain induced ferroelectricity [2], colossal magnetoresistance [3], etc. These unique properties, which their bulk counterparts do not possess, can be tuned by epitaxial strain [4], external electric or magnetic field [5–7] and chemical doping [8,9]. Meanwhile, structural defects such as dislocation, grain boundaries and the extended planar faults, which sometimes are inevitable, are also an important factor affecting the physical properties of the film. These defects can introduce a translational discontinuity into the crystal structure, change the electronic structure, and then passively affect the mechanical and electrical properties [10–13]. It is therefore necessary to identify these structural defects and find out their formation mechanisms, which no doubt will facilitate the development of film fabrication and interface engineering.

* Corresponding author at: Beijing National Laboratory of Condensed Matter Physics, Institute of Physics, Chinese Academy of Sciences, Beijing 100190, PR China; School of Physical Sciences, University of Chinese Academy of Sciences, Beijing 100049, PR China.

E-mail address: rcyu@iphy.ac.cn (R. Yu).

Of the transition metal oxide films, the LaCoO_3 (LCO) thin film has attracted great attention in recent years due to its unusual magnetic properties associated with the various spin states of the cobalt cation [14,15]. The spin states result from the competition between crystal field splitting and Hund's-rule coupling, and they can be tuned by changing temperature and/or introducing lattice strains [16–18]. For example, the high spin state ($t_{2g}^5 e_g^1$, $S = 2$) of Co^{3+} comes into being in the low spin (t_{2g}^6 , $S = 0$) Co^{3+} matrix under tensile strain [4,19]. Unlike LCO, the SrRuO_3 (SRO) is an itinerant ferromagnet with metallic conductivity. It has a larger lattice constant than LCO [20]. To find out the process of interlayer reconstruction and its effect on the magnetic properties of LCO, LCO/SRO multilayer thin films grown on the SrTiO_3 substrate are prepared and investigated. Nevertheless, the planar faults arise in the growth process, which may cause the properties of these films to significantly deviate from the expected properties.

In this research, we focus on the microstructures of the thin films through the Z-contrast image analysis by scanning transmission electron microscopy (STEM). The films contain Ruddlesden–Popper-type (R.P.) faults, which have been extensively studied in perovskite thin films with extra A cation [21–23], especially in the thin films grown on SrTiO_3 (STO) [24–26]. Our studies focus on R.P. faults microstructures in more detail to find out the atomic

arrangements of the extended R.P. faults, and provide suitable structure models for structural defects.

2. Experiments

The multilayer films with alternately stacked LCO/SRO layers were epitaxially grown on (0 0 1)-oriented SrTiO₃ substrate by pulsed laser deposition (PLD). The SRO and LCO deposition temperatures were 853 K and 953 K, respectively. During the deposition, oxygen pressure was fixed at 10 Pa. After the deposition, the samples were furnace-cooled to room temperature without changing the oxygen pressure. The adopted laser fluence was 2 J·cm⁻² and the repetition rate was 2 Hz. Fixing the layer thickness of LCO at 1.5 nm and changing the deposition thickness values of SRO of the two films (films 1 and 2) into 3 nm and 9 nm, respectively, two multilayer films of LCO/SRO with a stacking periodicity of 5 were obtained. Compressive stains in the multilayers were induced by STO and LCO due to their smaller lattice parameters (3.91 Å, 3.80 Å) than the parameter of SRO (3.93 Å) [27], while LCO thin films were in tension originating from the SRO layer. These thin films were investigated by aberration corrected high-angle annular dark-field (HAADF) scanning transmission electron microscopy imaging (STEM) on a JEOL-ARM200F.

3. Results and discussion

Fig. 1 shows the representative atomic cross-sectional HAADF images of two films along the [1 0 0] zone axis of STO. The arrows mark the planar faults, which interrupt the continuities of the perovskite-type structures in the films. The SRO layer in Fig. 1(c) is about three times thicker than that in Fig. 1(a), and the thickness values of LCO in these two films are almost the same. Since the intensity in HAADF image is approximately proportional to $Z^{1.7}$, where Z is the average atomic number in the atomic columns

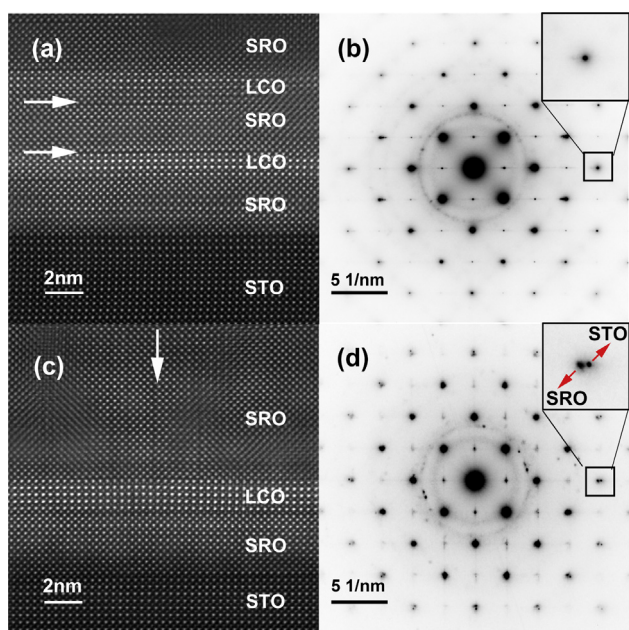


Fig. 1. (a) Cross sectional HAADF image of LCO/SRO multilayer thin film (LCO 1.5 nm, SRO 3 nm). (b) Corresponding SAED pattern including the contributions from both the film and the substrate in panel (a) along the [1 0 0] direction. (c) Cross sectional HAADF image of LCO/SRO multilayer thin film (LCO 1.5 nm, SRO 9 nm). (d) SAED pattern including the contributions from both the film and the substrate in panel (c) along the [1 0 0] direction. Insets in panels (b) and (d) show the magnified diffraction spots.

[28], the brightest spots correspond to the lanthanum atoms in the LCO layers. In the SRO layer, the spots weaker than those corresponding to the La atoms result from the ruthenium and strontium atom columns whose intensities differ from the intensity of the La atoms significantly because of the difference between their Z values. This allows us to distinguish the LCO from the SRO layers. Obviously, the bottom layers in Fig. 1(a) and (c) are SRO. The SRO and LCO are stacked alternately. The selected area electron diffraction (SAED) patterns containing the film and the substrate are shown in Fig. 1(b) and (d). Since the SRO and LCO layers in Fig. 1(a) are very thin, their contributions to the diffraction pattern of Fig. 1(b) are negligible. In this type of structure, most of the R.P. faults are parallel to the interface and located in the vicinity of interface of LCO/SRO and in the LCO layers. However, the lattice mismatch between SRO and STO can be revealed with increasing the layer thickness in SRO layers as reflected in the SAED (Fig. 1(d)). In addition, clear streak patterns appear in the SAED, indicating the formation of the R.P. type faults in the films.

3.1. Horizontal R.P. faults

Fig. 2(a) is a high-resolution cross-sectional HAADF image, which shows a typical horizontal R.P. fault located at the LCO/SRO interface. The insets show the intensities of line profiles, confirming that the extra atomic column at the interface could be La atom or/and Sr atom. Two possible situations in Fig. 2(a) are depicted by a three dimensional (3D) atomic model as indicated in Fig. 2(b), which exactly represents a comparatively small 3D inclusion surrounded by R.P. faults. The black lines show the locations of the R.P. faults. Generally, the La-O bottom layer (A-O layers) grows perfectly, and the subsequent plane should be Co-O or Ru-O layers (B-O layers) at the interface. A R.P. fault forms when further La atoms or Sr atoms are locally deposited on the nominal Ru-O or Co-O layer. In the cross-sectional view, the relative displacement between two adjacent La (Sr)-O planes separated by the planar faults is $a/2 [0 0 1]$ along the out-of-plane direction. This local stacking fault is likely to be due to small environmental variations in the growth process.

Fig. 2(c) shows a special region in the LCO layer with horizontal R.P. faults at the interlayers (marked by the red arrows). It is clearly observed in the insets that the two intensity profiles decrease and increase gradually, respectively. By carefully inspecting the relative brightness, the maximal and minimal intensities in the profiles correspond to La and Co atomic columns, respectively. The exchange in the intensity profiles also indicates that several R.P. faults are present in the transitional region in the LCO plane. According to the result mentioned above, we built a structural model as shown schematically in Fig. 2(d). When the additional LaO (1 0 0) or (0 1 0) plane is partially inserted into the film in a zigzag manner marked by the black line (z shape) (see the top plane in Fig. 2(d)), the crystal transitional region with the extra LaO layer shears a lattice translation vector $t = a/2 [1 1 1]$ [29]. It is visible that Co atoms are located on the rightmost side of the top layer, and La atoms occupy the positions of Co atoms step by step through inserting the extra La-O layers, and eventually Co atoms are totally displaced by La atoms. The red spheres in the cross section illustrated in Fig. 2(d) represent the projection image of the mixed column coming from La and Co atoms due to the R.P. faults. The z shape planar faults in LCO layers originate from the R.P. faults at the LCO/SRO interface (marked by red arrows in Fig. 2(c)).

3.2. Vertical R.P. faults

When the SRO layer thickness values increase up to 9 nm, the extra SrO plane appearing in the SRO films grows perpendicularly

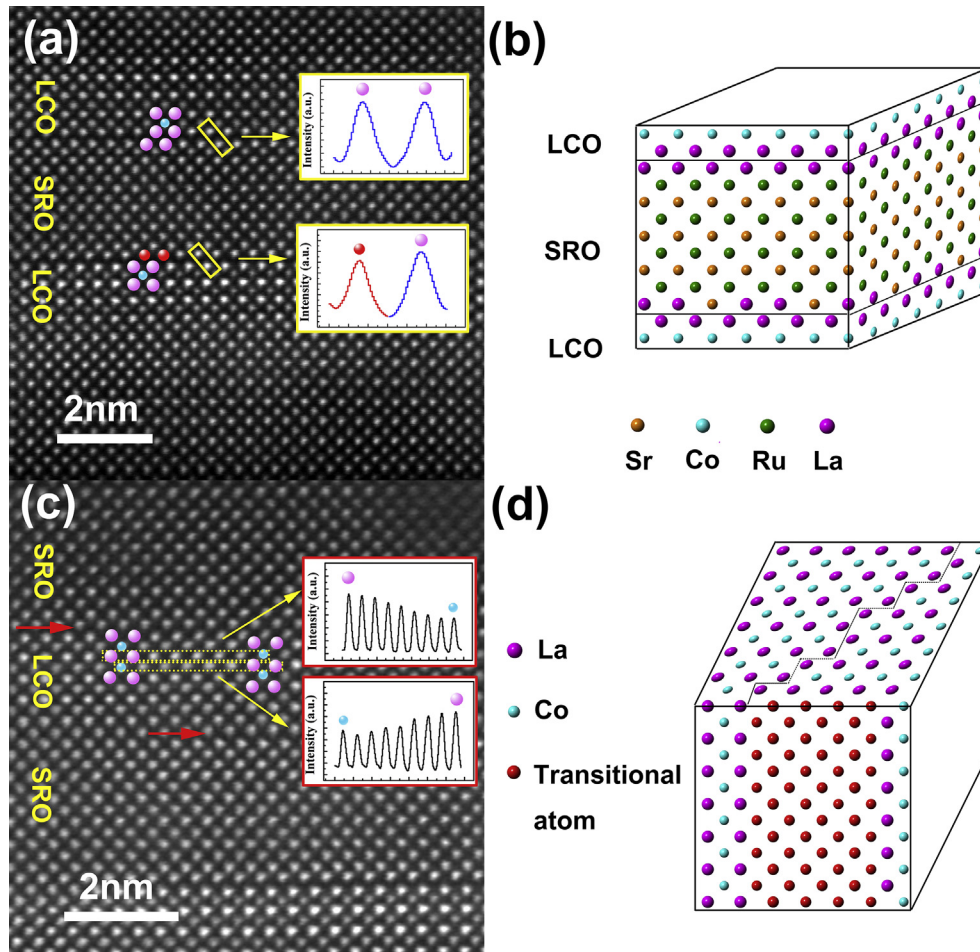


Fig. 2. (a) HAADF image with horizontal R.P. faults at the interfaces of LCO/SRO, with insets showing the intensity line profiles across the interfaces. (b) 3D atomic model of the planar faults in panel (a). (c) HAADF image with z-shaped R.P. faults in LCO layer, which are identified from the line profiles in insets. (d) 3D structural model nearby the planar faults in panel (c). La, Co, Sr, Ru atoms are denoted by purple, blue, orange and green spheres, respectively, and the red sphere represents the mixture of La and Sr atoms. (For interpretation of the references to color in this figure legend, the reader is referred to the web version of this article.)

to the interface. Fig. 3(a) shows a typical R.P. fault with an inserted extra SrO plane, and the corresponding atomic schematic diagram is shown in Fig. 3(b). In addition, Fig. 3(c) shows an area in the SRO film, where two vertical R.P. faults grow parallel to each other. Based on the line-profile intensities in the insets of Fig. 3(c), the types of atoms in regions (1) and (3) are not changed, but the intensities of the atomic columns in region (2) each remain at a steady level and they are stronger than that of the Sr atoms but weaker than that of the Ru atoms. According to the Z contrast analysis, we propose a probable structure (n shape) (Fig. 3(d)) for the particular region (2) between the observed two planar faults. The insertions of the extra SrO (1 0 0) and (0 1 0) planes cause the atomic columns to rearrange along the [0 1 0] direction and the region (2) to shift to a position that is overlapped with Sr and Ru atoms. Due to the rearrangement caused by the R.P. faults, the average atomic number Z will be in the middle of Sr and Ru atomic numbers.

In our experiment, the R.P. planar faults, which are parallel and perpendicular to the interface, are observed in two films respectively. The directions of planar faults depend on the extra number of A atoms. When the excess A atoms increase to a critical number, the growth direction of R.P. fault changes from normal to the surface to parallel to the surface [26]. However, in our case, the R.P. type faults are changed from parallel to the interface to normal to the interface with increasing the thickness of SRO layers, which

indicates that the formation of planar fault is dominated by the strain induced by the SRO layer.

Fig. S1 shows A-A atom horizontal distances in the LCO and SRO films. In Fig. S1(c), it is visible that the lattice parameter ($3.78 \pm 0.01 \text{ \AA}$) along the [0 1 0] direction in film 1 is close to the LCO lattice parameter, and, on the contrary, the lattice parameter ($3.91 \pm 0.02 \text{ \AA}$) is dominated by that of SRO in film 2. Due to the limited thickness of SRO in film 1, LCO/SRO can fully accommodate the strain ($\epsilon_{xx} = 3.38\%$ compressive strain) by the elastic deformation of the lattice. However, at the interface, the accumulated strain can affect the chemical stabilities of the elements [30].

As the thickness of SRO layer increases (9 nm), the strain in the film exceeds a critical value and is released through the formation of vertical planar faults. It is generally believed that the occurrence of R.P. faults is due to the advent of the excessive SrO planes in the SRO film [31]. Alternatively, this type of R.P. fault can also be regarded as a vertical dislocation with a RuO missing plane. This missing plane can reduce the in-plane lattice mismatch at a half unit cell size, and thus in principle allows the film to partially relax the compressive strain induced by the LCO film or the STO substrate.

The local lattice strain in the vicinity of the vertical fault is studied by applying Peak Pairs Analysis (PPA) to the SRO/LCO high resolution HAADF image in Fig. 4(a), which shows a Z-contrast image containing a vertical planar fault. Fig. 4(b)–(d) shows the strain

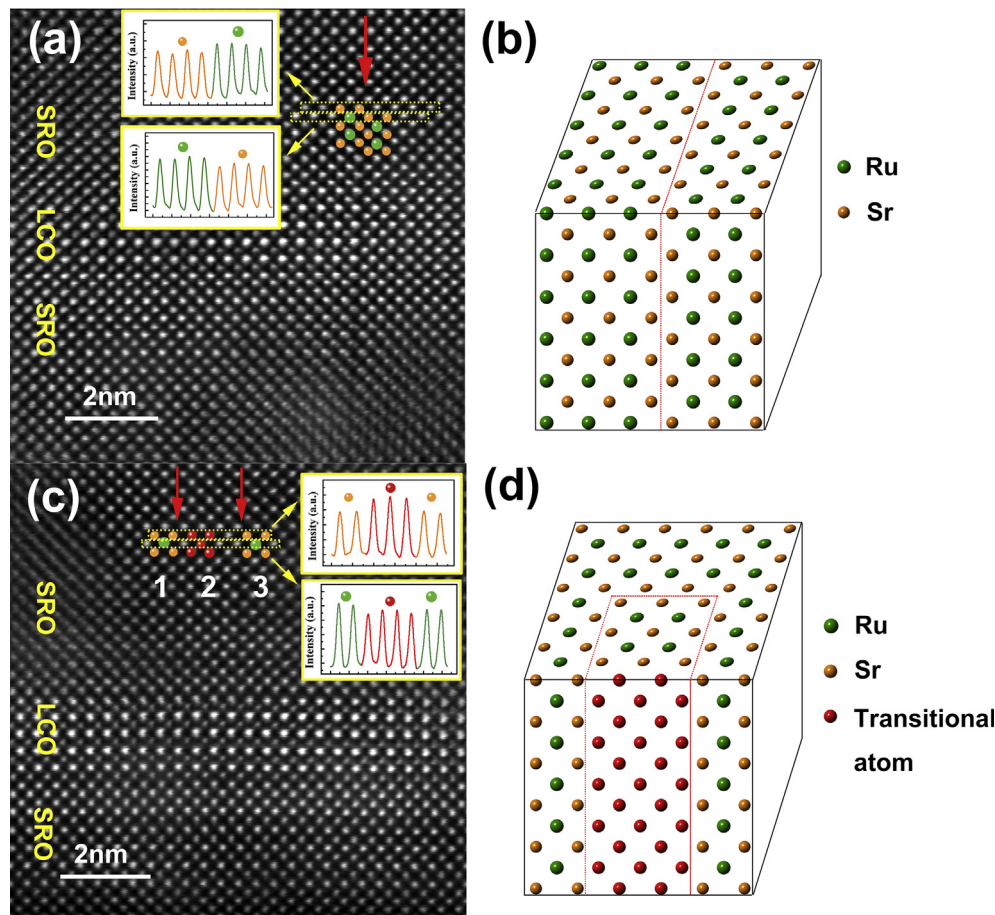


Fig. 3. (a) HAADF image with a vertical R.P. fault arising from the inserted extra SRO plane in the SRO layer, and showing the intensities of the line profiles as marked by the yellow dotted lines. (b) 3D atomic model of the planar faults in panel (a). (c) HAADF image with two vertical R.P. faults, which divide the SRO layer into three regions marked by 1, 2 and 3; with insets showing the intensities line profile marked by the yellow dotted lines. (d) 3D structural model containing the planar faults in panel (c). The Sr and Ru are denoted by orange and green spheres, respectively, and the mixture of Ru and Sr atoms by the red spheres. (For interpretation of the references to color in this figure legend, the reader is referred to the web version of this article.)

tensor components in Fig. 4(a). The strain tensor ε_{xx} corresponds to the strain along the interface, the strain tensor ε_{yy} reflects the strain parallel to the R.P. fault, and ε_{xy} corresponds to the shear term. The components of the 2D strain tensors are displayed with an intensity color scale. In order to inspect the effect deriving from the R.P. fault, a region far away from the defect is chosen to analyze the line profile (see the dash lines in Fig. 4(a)). A comparison in extracted line profile between in Fig. 4(b) and in Fig. 4(d) evidently shows that the SRO and LCO films are grown coherently along the $[0\ 1\ 0]$ direction because of the R.P. fault, but, on the contrary, the lattice parameters of SRO and LCO in the $[0\ 0\ 1]$ direction fluctuate remarkably due to the Poisson effect and the strain effect. The SRO in-plane lattice parameter is clamped by the LCO films, and is in compressive strain. According to the Poisson effect, SRO out-of-plane lattice parameter will be expanded. Moreover, the out-of-plane lattice parameter will fluctuate due to the strain relaxation, and R.P. faults and the strain combination of both sides LCO and STO in the films as the SRO film is away from the LCO layer (see Fig. 4(f)).

The strain in the multilayer thin film may arise from the lattice mismatch, and the difference in thermal expansion coefficient between the thin film and the substrate may also lead to a residual strain in the deposition process [32]. To indicate the residual strain caused by the difference between thermal expansion coefficients, the lattice parameters of LCO, SRO, STO and their corresponding lattice mismatches at room temperature and deposition

temperature are listed in Table 1. Due to the large thermal expansion coefficient of LCO, the lattice mismatch between LCO and SRO at deposition temperature is quite different from that at room temperature, which leads to a residual strain between the two layers (LCO/SRO) in the cool-down process. The additional strain can give rise to the chemical instability at the LCO/SRO interface and induce the planar faults to form.

4. Conclusions

In this work, the atomic structures of the R.P. faults in LCO/SRO multilayer grown on the STO substrate are revealed. Horizontal R.P. faults are detected at the LCO/SRO interface within the LCO layer, and they are generated by elemental fluctuations at interfaces due to lattice strains. Vertical R.P. faults are observed in the thicker SRO single layer, owing to the presence of excessive Sr, which reduces the strain effect according to the PPA analysis. Moreover, this type of planar fault exists only in thicker SRO layers. Possibly, the lattice strains relax in this manner. And it can be concluded that the growing direction of R.P. planar fault is closely related to the strain effect and could be changed with increasing SRO thickness. The proposed 3D structural models would give an easy access to the better understanding of the formation of R.P. faults, and our results could be helpful in adjusting the film growth condition. In addition, it should also be emphasized that the 3D structural

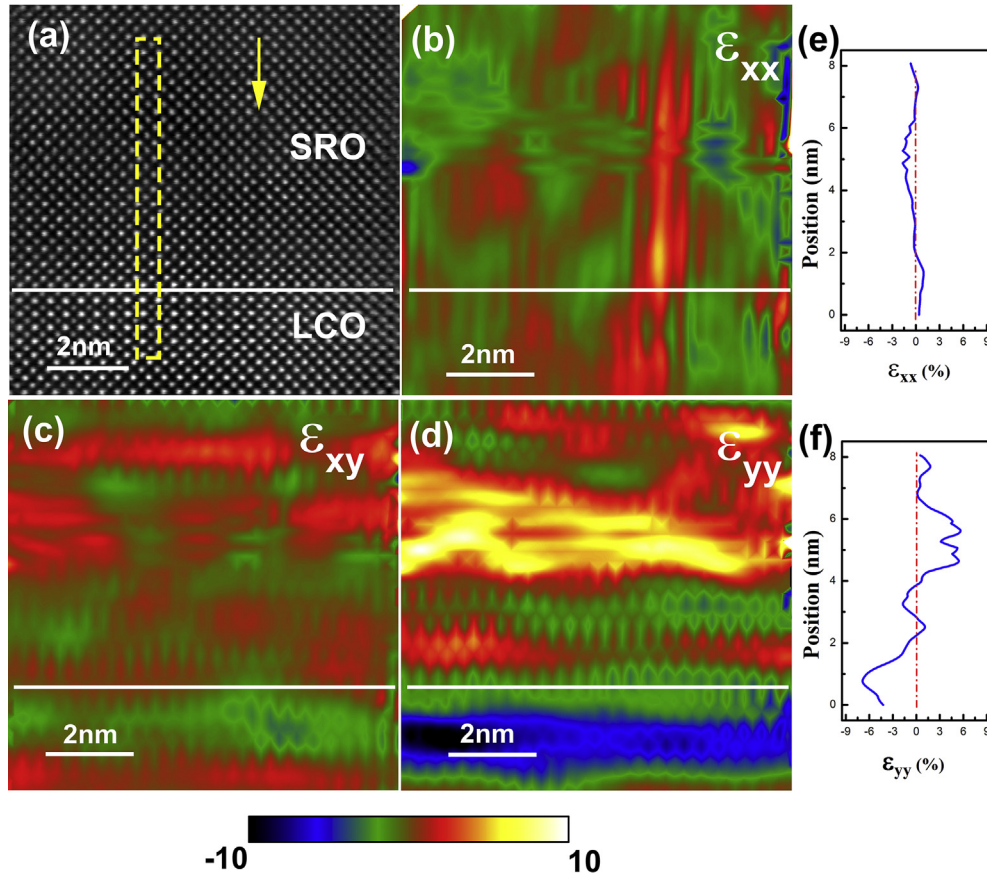


Fig. 4. PPA dataset. (a) Z-contrast STEM image showing one vertical planar fault. (b) ϵ_{xx} , (c) ϵ_{yy} , and (d) ϵ_{xy} , the 2D tensor components with intensity color scale, which are obtained by PPA from panel (a). (e) and (f) Line profiles of ϵ_{xx} and ϵ_{yy} in the area marked by the dashed rectangular frame in panel (a). Interfaces are marked by white solid lines. (For interpretation of the references to color in this figure legend, the reader is referred to the web version of this article.)

Table 1

Lattice parameters of a_{SRO} , a_{LCO} and a_{STO} , and the corresponding lattice mismatches, $\epsilon_1 = (a_{\text{SRO}} - a_{\text{STO}})/a_{\text{STO}}$ and $\epsilon_2 = (a_{\text{SRO}} - a_{\text{LCO}})/a_{\text{SRO}}$. The thermal expansion coefficients of SRO, LCO and STO are about $1.03 \times 10^{-5}/\text{K}$, $2 \times 10^{-5}/\text{K}$, $1 \times 10^{-5}/\text{K}$, respectively [4,33].

	a_{LCO} (Å)	a_{SRO} (Å)	a_{STO} (Å)	ϵ_1 %	ϵ_2 %
T = 300 K	3.80	3.93	3.91	0.64	3.8
T = 953 K	3.82	3.94	3.92	0.63	3.0

models for these R.P. faults need further confirming by theoretical calculations.

Acknowledgements

This work was supported by the National key research program of China (Grant Nos. 2016YFA0300701, 2017YFA0206200) and the National Natural Science Foundation of China (Grant Nos. 11574376, 11374343).

Appendix A. Supplementary material

Supplementary data associated with this article can be found, in the online version, at <https://doi.org/10.1016/j.jcrysgro.2018.03.029>.

References

- [1] A. Ohtomo, H. Hwang, *Nature* 427 (6973) (2004) 423–426.
- [2] J. Haeni, P. Irvin, W. Chang, R. Uecker, P. Reiche, Y. Li, S. Choudhury, W. Tian, M. Hawley, B. Craigo, *Nature* 430 (7001) (2004) 758–761.
- [3] M. Fäth, S. Freisem, A. Menovsky, Y. Tomioka, J. Aarts, J. Mydosh, *Science* 285 (5433) (1999) 1540–1542.
- [4] D. Fuchs, E. Arac, C. Pinta, S. Schuppler, R. Schneider, H.V. Löhneysen, *Phys. Rev. B* 77 (1) (2008) 014434.
- [5] A. Caviglia, S. Gariglio, N. Reyren, D. Jaccard, T. Schneider, M. Gabay, S. Thiel, G. Hammerl, J. Mannhart, J.-M. Triscone, *Nature* 456 (7222) (2008) 624–627.
- [6] C. Bell, S. Harashima, Y. Kozuka, M. Kim, B.G. Kim, Y. Hikita, H. Hwang, *Phys. Rev. Lett.* 103 (22) (2009) 226802.
- [7] N. Kida, H. Yamada, H. Sato, T. Arima, M. Kawasaki, H. Akoh, Y. Tokura, *Phys. Rev. Lett.* 99 (19) (2007) 197404.
- [8] A. Gozar, G. Logvenov, L.F. Kourkoutis, A. Bollinger, L. Giannuzzi, D. Muller, I. Bozovic, *Nature* 455 (7214) (2008) 782–785.
- [9] O. Yuli, I. Asulin, O. Millo, D. Orgad, L. Iomin, G. Koren, *Phys. Rev. Lett.* 101 (5) (2008) 057005.
- [10] K. Szot, W. Speier, G. Bihlmayer, R. Waser, *Nat. Mater.* 5 (4) (2006) 312.
- [11] S. Thiel, C. Schneider, L.F. Kourkoutis, D. Muller, N. Reyren, A. Caviglia, S. Gariglio, J.-M. Triscone, J. Mannhart, *Phys. Rev. Lett.* 102 (4) (2009) 046809.
- [12] V. Nagarajan, C. Jia, H. Kohlstedt, R. Waser, I. Misirlioglu, S. Alpay, R. Ramesh, *Appl. Phys. Lett.* 86 (19) (2005) 192910.
- [13] M. Arredondo, Q.M. Ramasse, M. Weyland, R. Mahjoub, I. Vrejoiu, D. Hesse, N. D. Browning, M. Alexe, P. Munroe, V. Nagarajan, *Adv. Mater.* 22 (22) (2010) 2430–2434.
- [14] P. Raccach, J. Goodenough, *Phys. Rev.* 155 (3) (1967) 932.
- [15] M. Korotkin, S.Y. Ezhov, I. Solovyev, V. Anisimov, D. Khomskii, G. Sawatzky, *Phys. Rev. B* 54 (8) (1996) 5309.
- [16] P.G. Radaelli, S.-W. Cheong, *Phys. Rev. B* 66 (9) (2002) 094408.

- [17] D. Fuchs, C. Pinta, T. Schwarz, P. Schweiss, P. Nagel, S. Schuppler, R. Schneider, M. Merz, G. Roth, H.V. Löhneysen, *Phys. Rev. B* 75 (14) (2007) 144402.
- [18] A. Herklotz, A. Rata, L. Schultz, K. Dörr, *Phys. Rev. B* 79 (9) (2009) 092409.
- [19] H. Seo, A. Posadas, A.A. Demkov, *Phys. Rev. B* 86 (1) (2012) 014430.
- [20] G. Koster, L. Klein, W. Siemons, G. Rijnders, J.S. Dodge, C.-B. Eom, D.H. Blank, M. R. Beasley, *Rev. Modern Phys.* 84 (1) (2012) 253.
- [21] S. Ruddlesden, P. Popper, *Acta Crystallogr.* 11 (1) (1958) 54–55.
- [22] W. Wang, Y. Tang, Y. Zhu, J. Suriyaprakash, Y. Xu, Y. Liu, B. Gao, S. Cheong, X. Ma, *Sci. Rep.* 5 (2015).
- [23] E. Detemple, Q. Ramasse, W. Sigle, G. Cristiani, H.-U. Habermeier, B. Keimer, P. Van Aken, *J. Appl. Phys.* 112 (1) (2012) 013509.
- [24] R.C. Haislmaier, G. Stone, N. Alem, R. Engel-Herbert, *Appl. Phys. Lett.* 109 (4) (2016) 043102.
- [25] C. Brooks, L.F. Kourkoutis, T. Heeg, J. Schubert, D. Muller, D. Schlom, *Appl. Phys. Lett.* 94 (16) (2009) 162905.
- [26] Y. Tokuda, S. Kobayashi, T. Ohnishi, T. Mizoguchi, N. Shibata, Y. Ikuhara, T. Yamamoto, *Appl. Phys. Lett.* 99 (17) (2011) 173109.
- [27] V.M. Longo, M.D.G.S. Costa, A.Z. Simoes, I.L.V. Rosa, C.O.P. Santos, J. Andrés, E. Longo, J.A. Varela, *Phys. Chem. Chem. Phys.* 12 (27) (2010) 7566–7579.
- [28] S. Pennycook, *Ultramicroscopy* 30 (1–2) (1989) 58–69.
- [29] H. Du, C.L. Jia, J. Mayer, J. Barthel, C. Lenser, R. Dittmann, *Adv. Function. Mater.* 25 (40) (2015) 6369–6373.
- [30] M. Arredondo, M. Weyland, M. Hambe, Q. Ramasse, P. Munroe, V. Nagarajan, *J. Appl. Phys.* 109 (8) (2011) 084101.
- [31] C. Jia, J.R. Contreras, J. Schubert, M. Lentzen, U. Poppe, H. Kohlstedt, K. Urban, R. Waser, *J. Cryst. Growth* 247 (3) (2003) 381–386.
- [32] W. Fang, C.-Y. Lo, *Sensors Actuators A: Phys.* 84 (3) (2000) 310–314.
- [33] S. Yamanaka, T. Maekawa, H. Muta, T. Matsuda, S.-I. Kobayashi, K. Kurosaki, *J. Solid State Chem.* 177 (10) (2004) 3484–3489.